Supporting Information

Confined Vertical Foaming Induces Graphite Crystal Orientation: Exceptional Isotropy of Thermal Conductivity and Anti-Leakage Properties for Phase Change Systems

Yu Qin,[ab†] Le Ding,[a†] Zhao Jiang,[a] Yafang Zhang,[ab] Chong Ye,[ab] Jinshui Liu,[ab] Yudi Zhang,[ab] M.-Sadeeq Balogun,*[a] and Ting Ouyang*[abc]

Table S1. The properties of the mesophase pitch.

Density ($g \cdot cm^{-3}$)	Softening point [a] (°C)	Solubility (wt%) [b]			Anisotropic content (vol%)
		TS	TI-QS	QI	
1.22	287	26.23	31.62	42.15	100

[a] the softening point was determined by Mettler Toledo DP90; [b] TS Toluene soluble, TI-QS Toluene insoluble but quinoline soluble, QI Quinoline insoluble.

Thermal analysis of MP

In determining a proper foaming temperature range for the Taguchi investigation, raw material characterizations of viscosity and thermogravimetric analysis were conducted meticulously. Understanding the viscosity properties of the pitch is imperative as it directly impacts its flowability, a pivotal factor for successful foam formation.[1] The viscosity-temperature curve (Figure 2a) exhibits a characteristic "U" shaped transition (decreases first and then decreases), within the range of 300 to 500℃, similar to findings in previous study.[2, 3] Initially, upon heating to the softening point, the pitch transforms into a molten state, leading to a notable decrease in viscosity. While the decrease of viscosity flattens from 350 to 450 ℃, as the temperature exceeds 450 ℃, viscosity begins to rise, coinciding with the rapid evolution of volatilization, polymerization, and condensation.[4] This increase in viscosity tends to capture the bubbles in place, facilitating foaming primarily in the unrestrained z-direction.[5] Thermogravimetry (TG) in combination with derivative thermogravimetry (DTG) (Figure 2b) reveals weight loss occurring within the temperature range of 350 to 580 ℃, indicating the release of gas, which serves as the foaming agent within the molten pitch. At higher temperatures the mesophase initiates pyrolysis (polymerization) and generating additional volatile species. This weight loss occurs simultaneously with an increase in molecular weight, contributing to the increased melt viscosity of the molten mesophase, aligns with the observed trend after 450 ℃ in the viscosity curve. It is foreseeable that as the temperature rises further, the foamed mesophase undergoes continued pyrolysis, leading to a gradual increase in viscosity until it reaches a state of being sufficiently cross-linked, making it infusible and impossible to melt.[6]

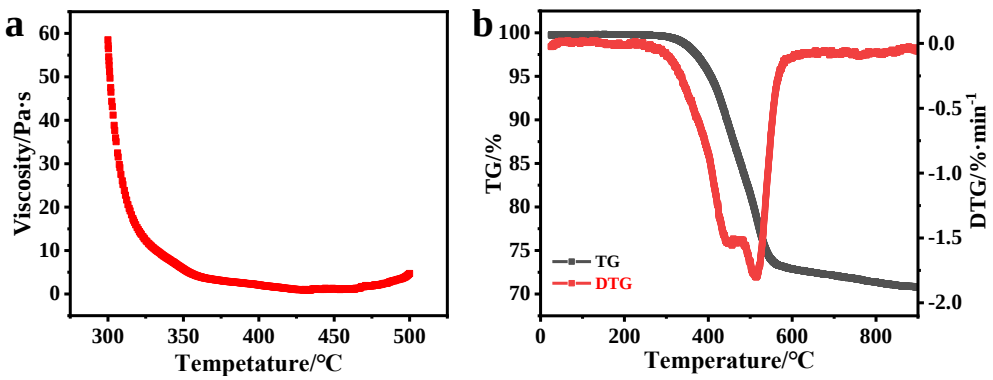

Figure S1. (a) Viscosity-temperature curves for pitch, (b) TG and DTG curves for pitch. Based on the findings, to conduct a comprehensive study of orthogonal experiments, the levels of factors were set both above and below the identified temperature range. Detailed information regarding the influential factors and their respective levels can be found in Table 2. The experimental design employed an $L_{16}(4^3)$ orthogonal array, resulting in varied GFBGF densities are as depicted in Table 4.

Design of Taguchi experiments

Table S2. Assignment of the levels to the factors.

Level	Heating rate /°C·min^{-1}	Foaming temperature /°C	Foaming Time /h
1	2	380	0.5
2	5	440	1.0
3	7	500	1.5
4	10	560	2.0

Table S3. Orthogonal array $L_{16}(4^3)$ of Taguchi.

$L_{16}(4^3)$	Heating rate /°C·min^{-1}	Foaming temperature /°C	Foaming time /h
#1	1	1	1
#2	1	2	2
#3	1	3	3
#4	1	4	4
#5	2	1	2
#6	2	2	1
#7	2	3	4
#8	2	4	3
#9	3	1	3
#10	3	2	4
#11	3	3	1
#12	3	4	2
#13	4	1	4
#14	4	2	3
#15	4	3	2
#16	4	4	1

Table S4. Summary of the properties of GFBGF from each run.

Run No.	Density /g·cm^{-3}	S/N for Density
#1	0.44	-7.05
#2	0.43	-7.27
#3	0.53	-5.58
#4	0.53	-5.44
#5	0.45	-6.98
#6	0.43	-7.29
#7	0.52	-5.73
#8	0.46	-6.71
#9	0.43	-7.37
#10	0.47	-6.51
#11	0.53	-5.54
#12	0.45	-6.98
#13	0.43	-7.41
#14	0.48	-6.32
#15	0.54	-5.22
#16	0.45	-6.94

Table S5. Analysis of ANOVA for density.

	GI [a]	Sum of Squares	Mean of Square	F-value	P-value
Rate Heating	3	0.001	0.0003	0.378	0.773
Foaming Temperature	3	0.019	0.0064	7.372	0.019
Foaming time	3	0.001	0.0003	0.399	0.759
Error	6	0.005	0.0008		
Total	15	0.026			

[a] GI: degree of freedom.

Statistical analysis of the Taguchi experiments

To assess the foaming effects, GFBGF density was evaluated. The average values of each factor at every level were calculated, and the mean effect assessment was obtained using Equation (1)：

$$\bar{F} = \frac{1}{m}\sum_{j=1}^{m} y_{ij} \tag{1}$$

where $\bar{F}$ is the mean effect of the i^{th} level of the factor, m is the number of data points at the i^{th} level of the factor, $y_{ij}$is the j^{th} data of the i^{th} level.

The assessment of the main effects of each factor was calculated by Equation (2)：

$$\Delta F = Max\{\bar{F}_1, \bar{F}_2, \bar{F}_3, \dots \bar{F}_n\} - Min\{\bar{F}_1, \bar{F}_2, \bar{F}_3, \dots \bar{F}_n\} \tag{2}$$

Where the n is the number of levels(n=4 in the experiment)， ΔF is main effect， The larger the F-value, the more significant the impact on the results.

The impact of the experimental results can be assessed using the Signal-to-Noise (S/N) ratio in the Taguchi method, where a higher value indicates favorable performance. The S/N ratio can be calculated using Equation (3) and (4)：

$$S/N = -10\,log(MSD) \tag{3}$$

$$MSD = \frac{1}{l}\sum_{i=1}^{l} \frac{1}{y_i^2} \tag{4}$$

Where, l is the number of experiments selected for calculating the (S/N)

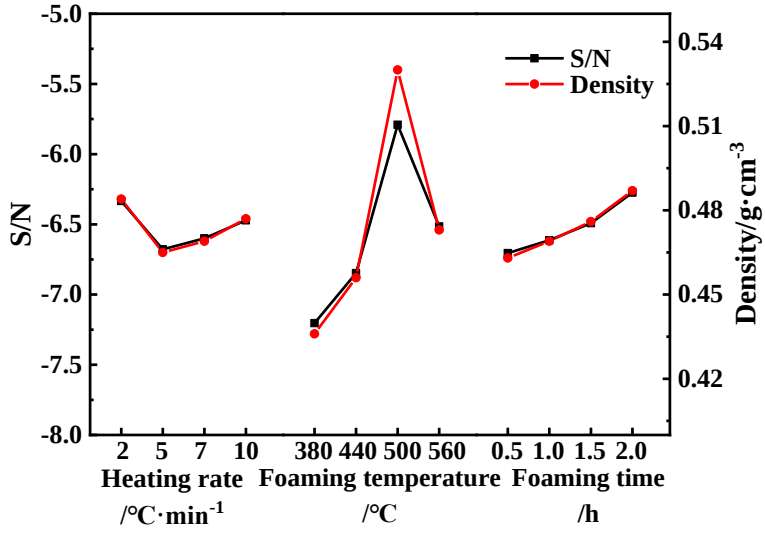

Figure S2. Main effect and mean effect of signal noise of S/N ratio.

Figure S2 illustrates the main effect and mean effect of the signal-to-noise (S/N) ratio. A larger S/N ratio signifies a more favorable outcome, reflecting the superior confined foaming effect on CBGF. The trend of the S/N value is the same at that of the mean density values at different levels, with both initially increasing before reaching maximum values at a foaming temperature of 500 ℃ (-5.79 for S/N and 0.53 g·cm^{-3} for density). This suggests that the optimal confined foaming densification effect occurs at a foaming temperature of 500 ℃. The initial rise in S/N and density can be attributed to the decreasing viscosity and intensified pitch pyrolysis between 380 ℃ and 440 ℃, resulting in the formation of numerous small bubbles. A slight increase in foam density from 0.43 to 0.48 g·cm^{-3} is facilitated by the increased volume fraction of dispersed gases and enhanced bubble entrapment. As the temperature increases from 440 to 500 ℃ the viscosity increases, hindering bubble movement and impeding melt within the GFBGF. The enhanced viscosity enables better retention of newly formed bubbles, preventing their coalescence and allowing them to remain dispersed within the pitch matrix, ultimately contributing to a denser foam structure of 0.54 g·cm^{-3}. By 560 ℃, the pyrolysis process may have progressed to a point where most of the volatile gases within the pitch have

been released. Consequently, limited bubbles are formed, exacerbating the increase in porosity and decrease in density to 0.45 $g \cdot cm^{-3}$. Therefore, it is speculated that at 500 ℃, the viscosity of the molten pitch reaches an optimal level where it balances the need for bubble growth and the resistance to bubble coalescence,[2] leading to the formation of a foam structure with an optimal balance of void space and solid material. Additionally, the foam structure at this temperature may exhibit improved structural integrity due to enhanced cross-linking of the pitch molecules, contributing to a higher overall density. In conclusion, foaming temperature emerges as the most influential factor based on the main effect analysis, with the optimal confined foaming effect observed at 500 ℃.

Table S6. Pore structure analysis using Mercury intrusion porosimetry

Sample	Density / g·cm^{-3}	Porosity / %	Averaged pore size /μm	Median pore size /μm
S13	0.43	81.1	24.7	83.9
S14	0.48	77.3	19.5	67.8
S15	0.54	76.6	4.8	87.5
S16	0.45	79.1	19.6	73.3

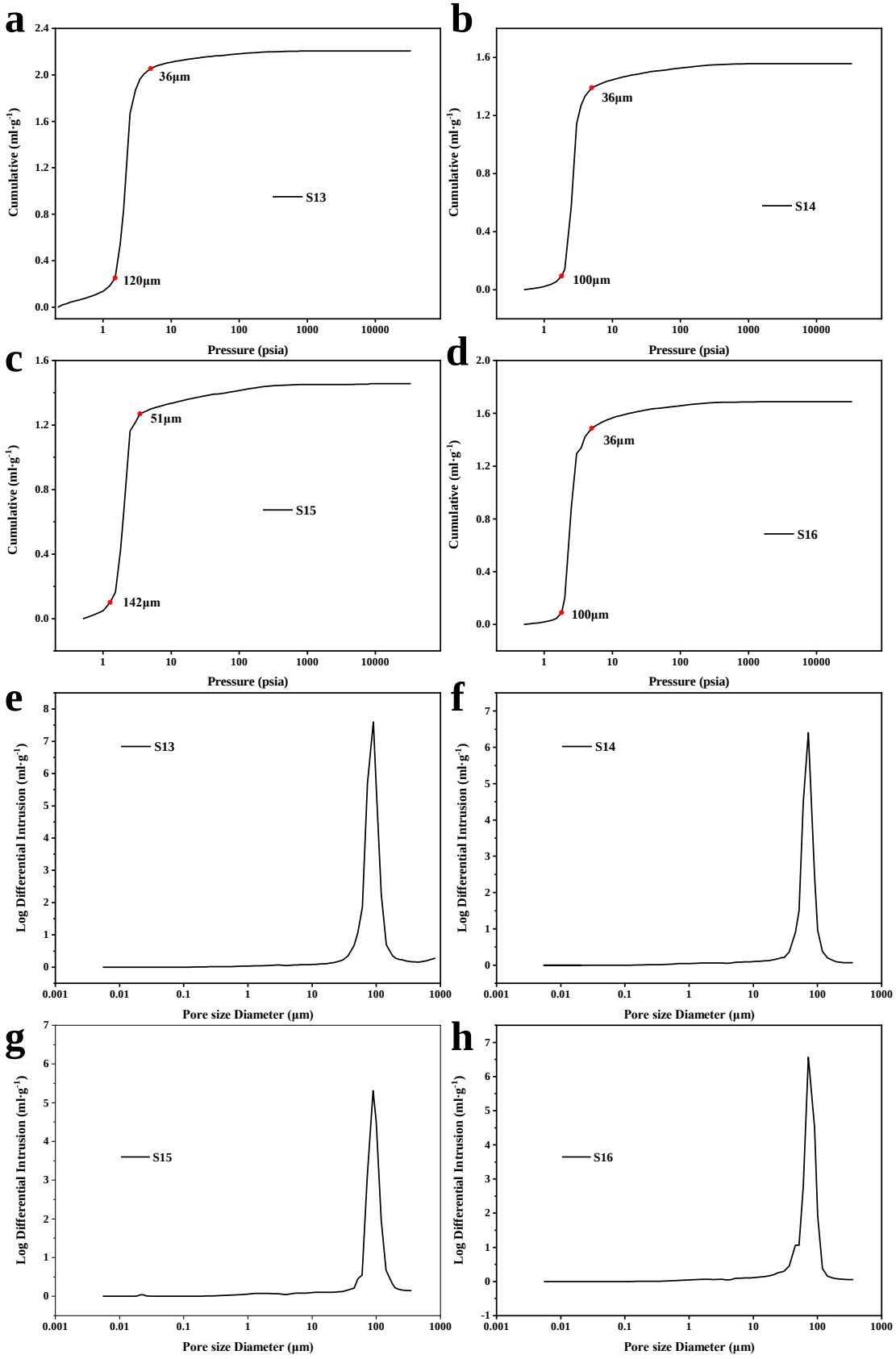

Figure S3. Mercury injection curve of S13(a). S14 (b). S15 (c) and S16 (d) .Pore density distribution chart of S13 (e). S14 (f). S15 (g) and S16 (h).

Microstructural characterization using Raman and XRD

Raman and XRD analyses were performed to assess the microstructural characteristics of GFBGF samples.

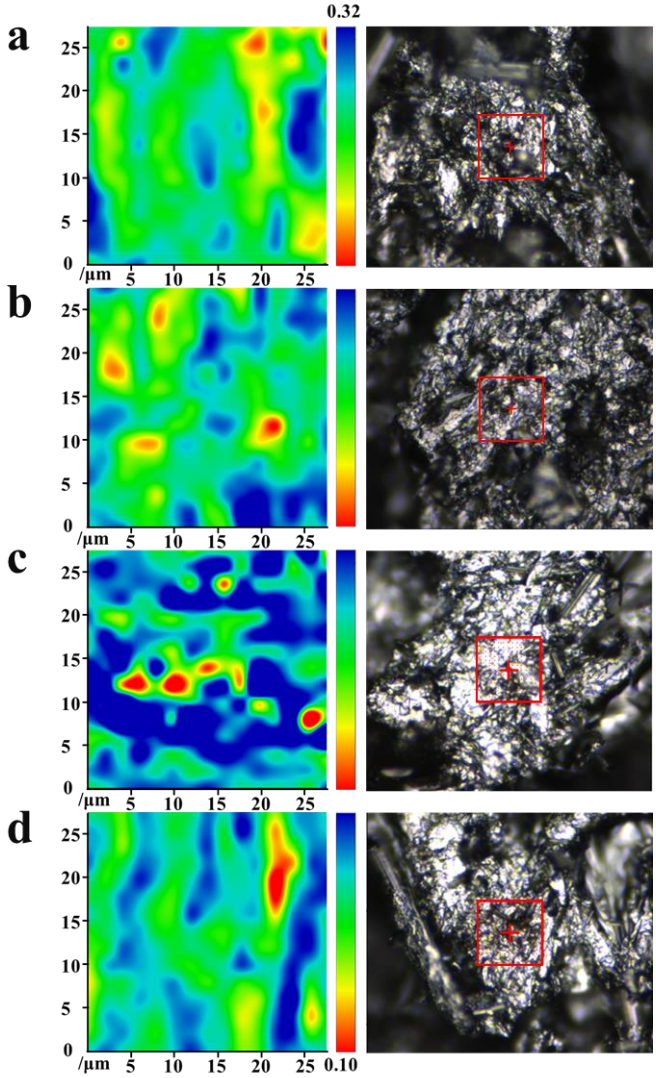

Figure S4. Raman I_D/I_G maps and optical pictures of (a-1) S13, (a-2) S14, (a-3) S15, (a-4) S16.

In Figure S3, I_D/I_G maps of the foam cell structure alongside optical micrographs of samples S13 to S16 reveal varying color distributions, indicating uneven graphitization degree across the tested area. Such variations are typical in carbon materials due to the orientation and growth of microcrystals in carbon foam, resulting in different distributed defects and graphitization degree.[7, 8]

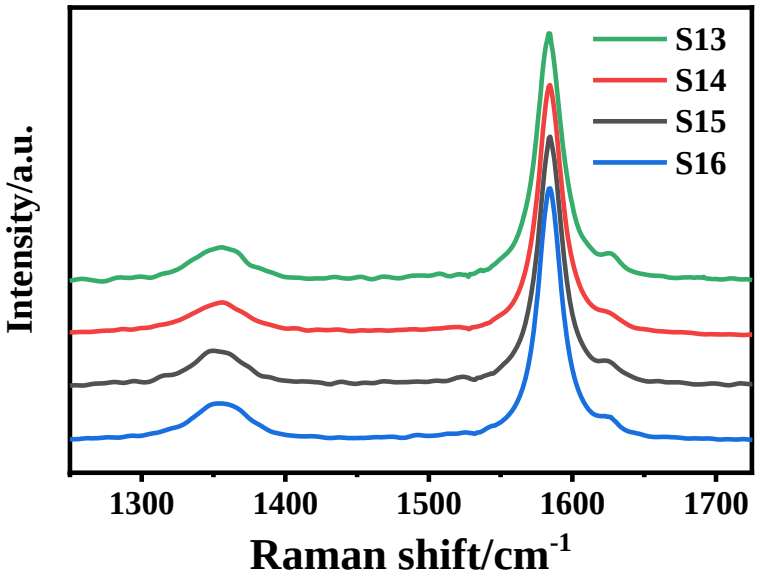

Figure S5. The averaged Raman spectrum for each sample.

The averaged Raman spectra in Figure S4 demonstrate consistent patterns of all GFBGF samples, with calculated I_D/I_G values around 0.16, suggesting a high level of graphitization comparable to commercial graphite.

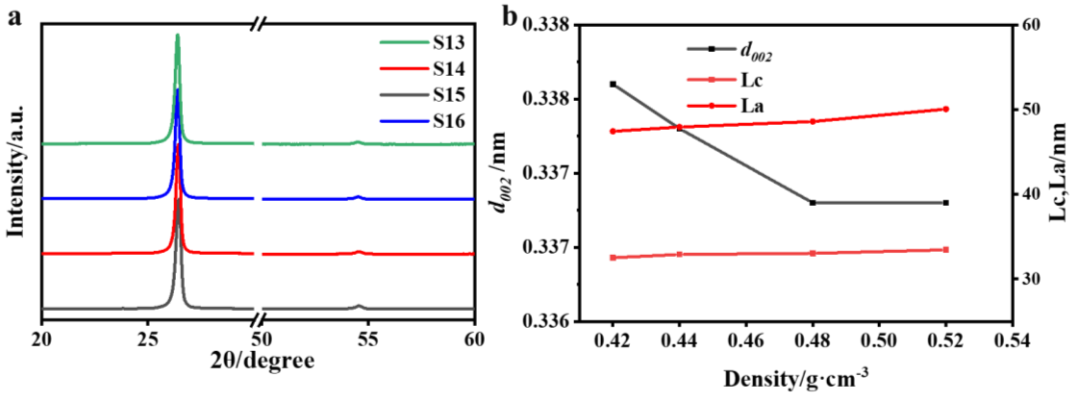

Figure S6. (a) XRD spectra, and (b) crystal parameters of the GFBGF samples.

XRD results (Figure S5a) exhibited distinct diffraction peaks corresponding to graphite crystal planes, with sample S15, possessing the highest density, showing larger graphite crystallite sizes (L_c and L_a) and smaller interlayer spacing (d_{002} = 0.337 nm) (Figure S5b). These differences are attributed to variations in pyrolytic carbon content of low graphitization degree, particularly evident in lower-density samples (S13, S14, and S16), where the higher proportion of phenolic resin derived pyrolytic carbon presented.[9] Overall, Raman and XRD analyses emphasize the significant graphitization of GFBGF, crucial for enhancing TC across the structure of PCM composite.

Table S7. Thermal properties of carbon-supported paraffin wax composites

PCC	Filler loading (vol%)	Filler loading (wt%)	TC(xy) (W/m·)	TC(z) (W/m·K)	ΔH (J/g)	REF
S13-PCM	19.32	36.92	22.43	11.19	121.96	This work
S14-PCM	20.23	38.26	26.65	13.82	119.00	
S15-PCM	21.86	40.62	28.25	16.51	117.60	
S16-PCM	24.70	44.49	33.05	18.76	107.20	
CF/PW	20.30	38.60	13.83	1.31	122.00	10
CF/PW	29.30	49.70	21.03		94.92	11
CF/PW	8.34	20.00	5.63	0.77	124.50	12
GNP/PW	23.08	40.00	32.80	9.80	99.75	13
Expanded graphite/ PW	20.10	30.00	10.48	5.83	128	14
Graphite foam/PW	53.50	59.90	19.27		90.30	15

References

1. M. Inagaki, J. S. Qiu and Q. G. Guo, *Carbon*, 2015, **87**, 128-152.
2. S. Z. Li, Y. M. Tian, Y. J. Zhong, X. Yan, Y. Song, Q. G. Guo, J. L. Shi and L. Liu, *Carbon*, 2011, **49**, 618-624.
3. W. Q. Li, H. B. Zhang and L. Y. Xia, *J. Porous Mater.*, 2015, **22**, 565-570.
4. N. Miyajima, T. Akatsu, O. Ito, R. Sakurovs, S. Shimizu, M. Sakai, Y. Tanage and E. Yasuda, *Carbon*, 2001, **39**, 647-653.
5. J. W. Klett, *Carbon*, 2019, **144**, 43-54.
6. D. G. T. e. E. D. H. Member, *Introduction to the Signal-to-Noise Ratio*, Taguchi's Quality Engineering Handbook, 2007.
7. J. W. Klett, A. D. McMillan, N. C. Gallego and C. A. Walls, *J. Mater. Sci.*, 2004, **39**, 3659-3676.
8. B. Fathollahi and J. Zimmer, *Carbon*, 2007, **45**, 3057-3059.
9. K. Kanno, N. Koike, Y. Korai, I. Mochida and M. Komatsu, *Carbon*, 1999, **37**, 195-201.
10. Z. Jiang, T. Ouyang, Y. Yang, L. Chen, X. Fan, Y. Chen, W. Li and Y. Fei, *Mater. Des.*, 2018, **143**, 177-184.
11. Z. Jiang, T. Ouyang, L. Ding, W. Li, W. Li and M.-S. J. T. Balogun, *Chem. Eng. J.*, 2022, **438**, 135496.
12. P. Zhang, Y. Qiu, C. Ye and Q. Li, *Chem. Eng. J.*, 2023, **461**, 141940.
13. S. Wu, T. Li, M. Wu, J. Xu, Y. Hu, J. Chao, T. Yan and R. Wang, *J. Mater. Chem. A*, 2020, **8**, 20011-20020.
14. Z. Huang, M. Liu, H. Chen, J.-N. Tang, X. Ouyang and D.-Z. Chen, *Energy Convers. Manage.*, 2022, **252**, 115078.
15. X. Yang, C. Li, Y. Ma, H. Chi, Z. Hu and J. Xie, *Chem. Eng. J.*, 2023, **473**, 145364.